Composite Structures 271 (2021) 114071

Contents lists available at ScienceDirect

Composite Structures

journal homepage: www.elsevier.com/locate/compstruct

Impact model of the Al_2O_3/ZrO_2 composite by peridynamics

Eligiusz Postek [a], Tomasz Sadowski [b,*]

[a] Institute of Fundamental Technological Research. Polish Academy of Sciences, PL-02-106, Poland
[b] Lublin University of Technology, PL-20-618 Lublin, Poland

ARTICLE INFO

Dedicated to Professor Holm Altenbach on the occasion of his 65th birthday

Keywords:
Al_2O_3/ZrO_2
Brittle composite
Peridynamics
Impact loading

ABSTRACT

Ceramic composites (CCs) are mixtures of different phases, and their development is often regarded as a milestone in technological progress. They are used in practically all significant industries. Frequently, CCs are exposed to variable dynamic loads, impacts or high temperatures [1–3]. In this paper, the impact of thin plates fabricated from Al_2O_3/ZrO_2 is analyzed. The plates are made of the above CC with different proportions of its components. Damage progression is analyzed using peridynamics, similarly to quasi-static tension [4]. The purpose of the study is to describe the impact damage development in the CC plates and determine the role of phase contents. It has been found that phase ratios in the tested CC are vital for the behavior of the plates. In conclusion, it can be claimed that the employed peridynamic approach is suitable for solving the problems under study and that the impacting plates should be treated as real three-dimensional structures.

1. Introduction

Multiphase Ceramic Composites (CCs) [1–11] are widely used in different branches of modern industry. The development of novel manufacturing technologies for multiphase has made it possible to fabricate internal structures with very complex morphologies. Using advanced technological methods one can create innovative composites with ordered internal structures, which is crucial for their future engineering applications in various structural elements under different loading processes (e.g. [90–104]) CCs can be manufactured with different internal phase morphologies, in regular or irregular forms, having:

- homogeneous distribution of multiphase components in CCs;
- layered structures having a regular or irregular arrangement;
- one-dimensional or multi-dimensional functional gradation of physical and mechanical properties.

Even single-phase ceramic polycrystals can be treated as CCs because they have a complex internal architecture, which results from the presence of interfaces with completely different mechanical and fracture resistance properties in comparison to grains, e.g. [12,13]. Much more complex internal structures are exhibited by porous [14–16], multiphase CCs [17–20], nanoceramic materials, [21,22] or functionally graded CCs with various gradation profiles, e.g. [22–36]. In all cases, the internal architecture of CCs can be artificially fabricated to control both physical and mechanical properties. Another class of advanced CCs widely used in different branches of industry comprises polycrystals composed of ceramic crystal WC or MoC bounded with Co or Ti metals, [37–47].

The behavior of CCs can be modelled using a multiscale method under which the problem is decomposed into several scales, [48–58]. In the classical approach, this is done using the two-scales method, i.e. one can distinguish a coarse- and a fine-scale [8–13,15–20]. Both scales are coupled by different discretization methods. One of them, particularly important for smeared crack growth, is the partition-of-unity method, e.g. [53,54]. For the case of dynamic loading of CCs, the peridynamic approach seems to be appropriate, [4].

Different kinds of CCs are applied for manufacturing critical structural parts in airplane or cars factories [59] or in nuclear power plants and aerospace industry [60,61]. For these applications, CCs must be modelled under extreme loading conditions such as impacts, high-velocity loads, elevated temperatures and thermal shocks.

Peridynamics is a relatively recent nonlocal, meshless method used for deformation state assessment. For the description of crystal behavior, a nonlocal approach was developed in [62,63]. For solving coupled problems, a generalized approach was proposed in [64]. The theory of peridynamics was originally elaborated by Silling [65,66]. Its application to modelling of quasi-brittle composites or metallic

* Corresponding author.
E-mail address: t.sadowski@pollub.pl (T. Sadowski).

https://doi.org/10.1016/j.compstruct.2021.114071
Received 13 April 2021; Revised 3 May 2021; Accepted 5 May 2021
Available online 8 May 2021

foams was described in [4] or [67]. A review of studies on peridynamic modelling of material failure is presented in [86]. Industrial applications of the peridynamic model are shown in, for example [87,88].

The contact algorithm between separate bodies is a generalization of contact between every calculation point [80–82]. The formulation for contact forces is given in [79,85,83]. Typically, the algorithms for searching contact between bodies are similar to those used in commercial programs, for example, [83–85].

In this study, an impact model for two variants of an Al_2O_3/ZrO_2 thin plate is numerically analyzed using the peridynamic approach. Both ceramic phases are described, including ~~a~~ brittle damage related to time and impact loading threshold [4,17–20]. The study focuses on modelling ~~of~~ damage initiation and location in the impacting thin plate, and the limitation of its further progression by the damage front line.

2. Problem solution method

In peridynamics, the elastic model is defined similarly to the continuous model [11] but made dependent on peridynamic states, [68].

Considering Fig. 1, **Q** and **x** are the points in the body in its initial configuration. The bond definition is:

$$\xi = Q - x \tag{1}$$

The reference state **X** is a function that is valid on the bond **X**($\boldsymbol{\xi}$). The deformation state is dependent on the new position of the coordinate$\boldsymbol{x}$ in the deformed body $y(\boldsymbol{x})$ in the following way:

$$\mathrm{Y}(x,\xi) = y(x+\xi) - y(x) \tag{2}$$

$$\mathrm{Y}(\mathrm{x},\xi) = y(Q) - y(x) \tag{3}$$

The state of displacements is:

$$\mathrm{U}(x,\xi) = u(x+\xi) - u(\xi) \tag{4}$$

$$\mathrm{U}(x,\xi) = u(Q) - u(x) \tag{5}$$

The scalar extension state e(**Y**) shown in Fig. 1 is of the form:

$$e(Y) = |Y| - |X| \tag{6}$$

The decomposition of the scalar extension state into spherical and deviatoric components, e^i and e^d, can be expressed as:

$$e = e^i + e^d \tag{7}$$

The force state t(**Y**) is shown in a form similar to the stress–strain relation that is the sum of its spherical and deviatoric parts, Eq. (7):

$$t(Y) = \left(\frac{3k\theta}{m}\right)\omega x + a\omega e^d \tag{8}$$

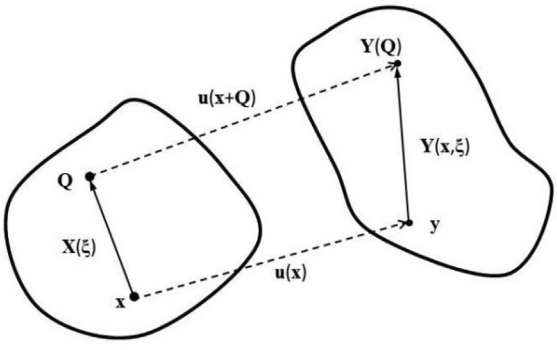

Fig. 1. Deformation of a body.

The k is the bulk modulus, θ is the dilatation, m is the weighted volume, ω is the influence function, $x = |\xi|$ is the basic scalar state, $\alpha = (15\mu)/m$ is the coefficient being in relation to the shear modulus μ.

The material failure model is based on the following assumptions: the bonds fail when their elongation overcomes the critical elongation; the total damage is due to the accumulating of broken bonds; and the bond breaking is irreversible.

A special case of the state-based model is the bond-based model [65,68,74]. A relationship between force and bond elongation is given in Fig. 2(b). It reads:

$$f = ce\varsigma(x,t,\xi) \tag{9}$$

where $c = (18k)/(\pi h^4)$ depends on the bulk modulus k and the horizon h. The force reaches its maximum value when the bond elongation is lower than the critical elongation e_{cr} and it is equal to 0 when the critical elongation is exceeded. The function ς is equal to 1 when the elongation is lower than the critical elongation of the bond and it is equal to 0 if the elongation is equal to its critical value. In our case, since the failure is predominantly assumed on cracks appearance, the e_{cr} evaluation is based on fracture energy evaluation, [66,4]. It reads:

$$e_{cr} = \sqrt{\frac{5G_{ci}}{9kh}} \tag{10}$$

where G_{ci} is the fracture energy depending on the mode of failure.

Following the above, for the special case, the dynamic equation of equilibrium can be written as:

$$\rho\ddot{u}(x,t) = \int_{\Omega} f dV + b(x,t) \tag{11}$$

where ρ is the material density, **f** is the forces vector f, $\mathbf{b} = \{b_i \ldots b_n\}$ is the body force density field. The equation of motion is integrated over the domain Ω.

The damage definion d reads:

$$d(x,t) = 1 - \frac{\int_{\Omega}\varsigma(x,t,\xi)d\Omega}{\int_{\Omega} d\Omega} \tag{12}$$

The damage variable varies between 0 and 1. The value 0 means that the material is pristine while 1 means that the material is completely damaged.

3. Materials and computational model

Al_2O_3/ZrO_2 composites used in the industry have different contents of their components, from pure Al_2O_3 up to a low content of alumina. An experimental analysis of these composites is presented in [17]. It has been found that the composites with a predominance of Al_2O_3 exhibit higher hardness, higher Young's modulus and lower crack resistance in contrast to the composites with a predominance of the ZrO_2 phase. Therefore, composites with a high content of Al_2O_3 are used in applications requiring high Young's modulus and higher hardness, for example in cutting applications or thin coating layers. Composites with a high ZrO_2 content can be used where higher compliance is required. These applications include ballistic shields and spacecraft constructions. When constructing a functionally graded material (FGM) that resists an impact, the outermost surface of the composite can consist of pure Al_2O_3, its contents gradually decreasing in the lower layers perpendicular to the axis of the impact [76]. Therefore, we have chosen two kinds of composites for analysis in this study. Following the approach adopted in [77] where the methodology is developed, this study presents a damage analysis of the plates.

A schematic design of the system is given in Fig. 3(a). A sample with the dimensions of 200 μm × 200 μm × 10 μm impacts a ~~fixed~~ elastic barrier. An initial velocity V is in the interval 10 m/s to 60 m/s. The barrier is fixed on its z-x outer surfaces. A SEM image of a microstructure is given in Fig. 3(b). The fair grains are the ZrO_2

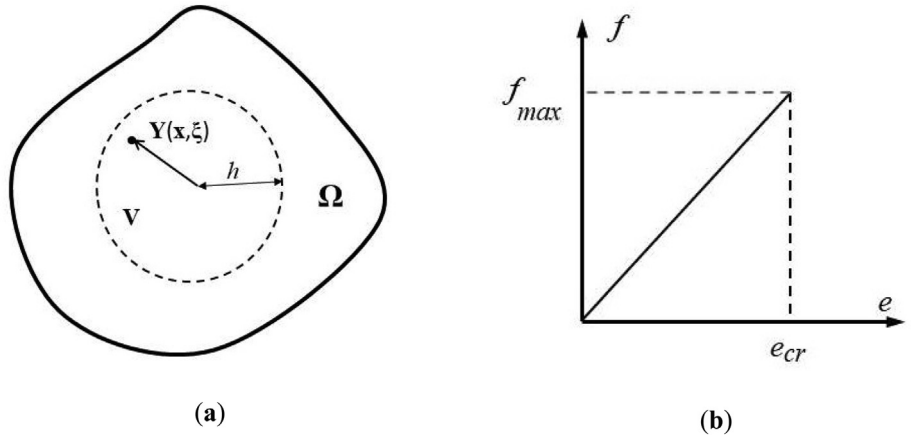

Fig. 2. Integration scheme (a), constitutive law (b).

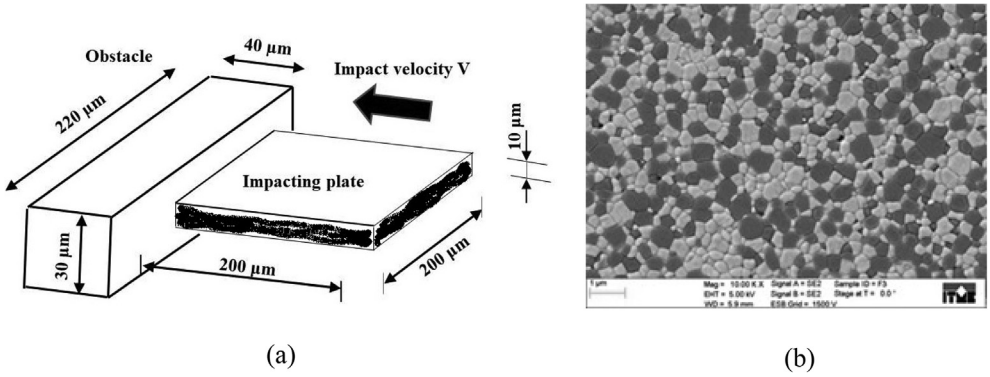

Fig. 3. Analyzed microstructure: (a) scheme of the analyzed mechanical system; (b) SEM image of an example of an Al_2O_3/ZrO_2 composite microstructure.

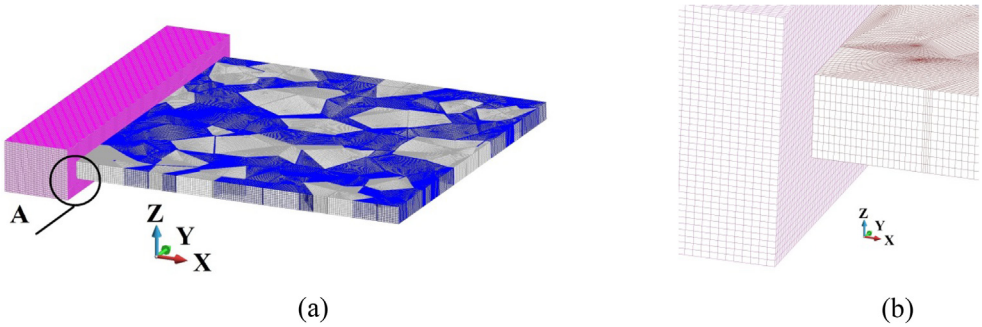

Fig. 4. Hexahedral discretization (a) entire structure; (b) detail A.

material, and the grey grains indicate Al_2O_3. Mechanical properties of the phases are given in Table 1.

The above values were obtained from the AZOM database of material properties for Al_2O_3 [69] and ZrO_2 [70], and [17]. The properties of both materials vary significantly. According to the provided data, Young's modulus for alumina ranges between 215 GPa and 413 GPa, whereas Young's modulus for zirconia varies between 100 GPa and 250 GPa. In this study, the extreme values of these properties are taken: the highest Young's modulus for alumina and the lowest Young's modulus for zirconia.

Table 1
Mechanical properties of the analysed phases.

	Al_2O_3	ZrO_2
Young's modulus (GPa)	413	110
Poisson's ratio	0.21	0.22
Mass density (kg/m^3)	3980	5000
Maximum tensile stress (GPa)	665	115
Crushing stretch $-e_{cr}$	1.610E−03	9.563E−04

The target is made of steel having Young's modulus of 211 GPa, Poisson's ratio of 0.3 and mass density of 7800 kg/m^3. Two cases of target microstructure are considered: with a low and high content of Al_2O_3, Fig. 6(a) and (b). The Al_2O_3 material is marked in grey, while ZrO_2 is marked in blue. The tested Al_2O_3 content is 41% and 75%, respectively. In Fig. 6(a) and (b) are marked 4 points where the damage is observed at the points and below. The points are chosen such that they are located approximately in the middle of particular crys-

tals. They are located in crystals of the same materials. One can observe a difference in particular field variables when, for example, Point A (ZrO_2) in Case A becomes surrounded by the crystals of Al_2O_3 in Case B. Other points are arranged in the same manner. Therefore, it is possible to follow changes occurring at particular points when the plate's composition is augmented by the addition of a higher content of the Al_2O_3 phase.

A computational model is built using peridynamics. The plate and the barrier are discretized with 1,319,160 and 640,00 volumes, respectively. The hexahedral discretization is shown in Fig. 3(a). Details of the contacting bodies are shown in Fig. 3(b). The plate and the barrier can be in general contact. This means that the search for contact is performed between all external surfaces of the objects, the self-contact being included too. A sphere is assumed around a calculation point. Inside the sphere, there is an icosahedron whose facets create contact surfaces. The contact is searched between the facets surrounding the points [78]. A penalty formulation is used. The friction coefficient is set to 0.3. An initial gap of 1 μm between the impacting plate and the barrier is applied.

The conversion of a fictitious sphere with a radius r_r in which the contact is searched is shown in Fig. 5(a). Since the contact is checked between the triangular facets of the bodies that are contact candidates, the sphere is transformed into an icosahedron, Fig. 5(b), inscribed into the sphere.

The contact is a force calculated based on a short-range force approach [66] and reads:

$$f_{ct} = \begin{cases} C_t(r_r - d)V_1V_2 & \text{for } d \leqslant r_r \\ 0 & d > r_r \end{cases} \tag{13}$$

where d is the distance between the bodies, V_1 and V_2 are the volumes associated with the corresponding calculation points and $C_t = 18\text{-}K_s/\pi h^5$. The constant Ks is the artificial spring stiffness assumed as a high penalty number of the range 1.0E + 12 ÷ 1.0E + 20. Eq. (13) is analogous to Eq. (9).

An important aspect of the model is the phase boundary. In the program, there are two bonds for any two interacting points. The total interaction between the points is the sum of the two bonds. Having two materials, the interaction is the average of two partial interactions.

A dynamic solver [71] is used in the calculations. The system was tested on several examples, so it can be regarded as highly reliable [75,81,89]. The total time is 4.0E-08 s. The explicit time integration is used, with a constant time stepping of 5.0E−811 s. The time step assuring the stability of the solution is 8.9E-11 s, which is well above the time step used. The solution requires 800 time steps. The horizon should be two to three times the distance between calculation points [71–73]. Although higher values of the horizon would not deteriorate the results [74], the computational time might become excessively long. The horizon is determined by the largest distance between the

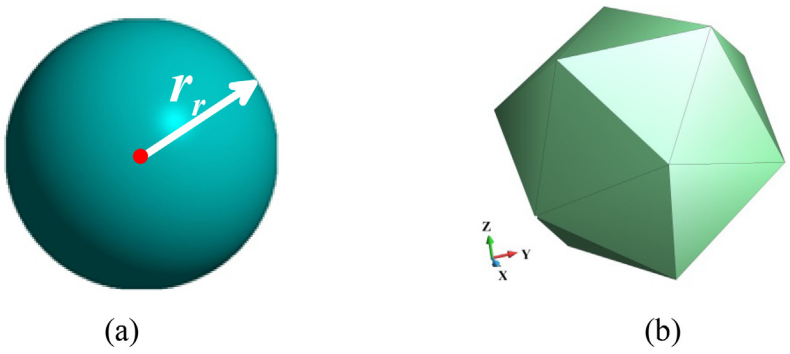

Fig. 5. Transformation of a sphere into an inscribed icosahedron: (a) sphere; (b) icosahedron.

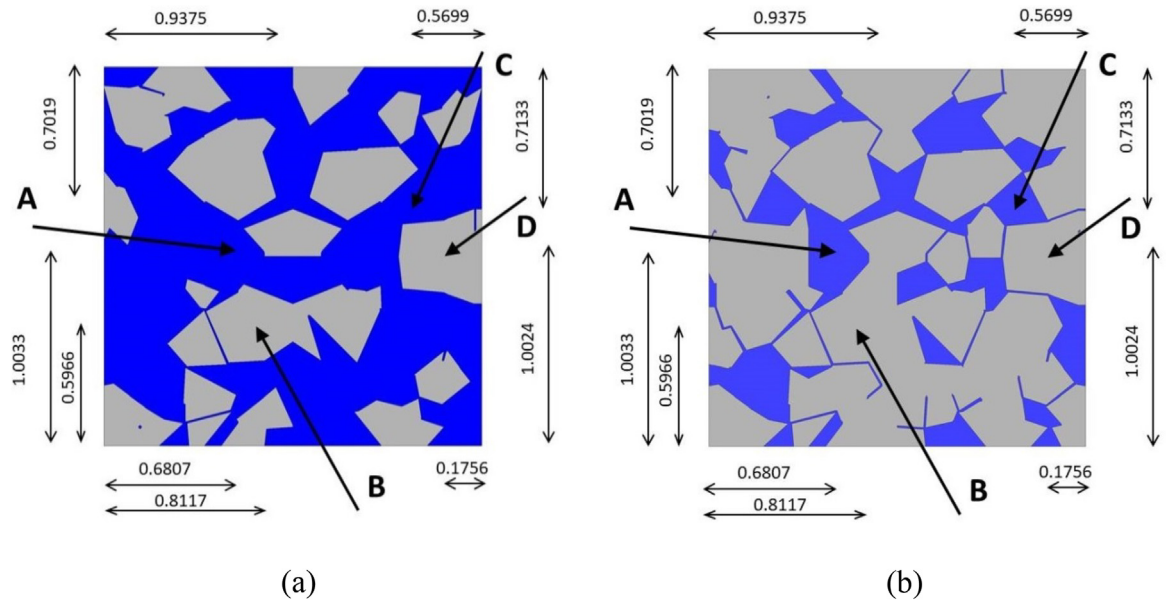

Fig. 6. Schemes of the analyzed samples (dimension × 1.0E−07 m), Al_2O_3 – grey, ZrO_2 - blue: (a) Low content of Al_2O_3, Case A; (b) High content of Al_2O_3, Case B. (For interpretation of the references to colour in this figure legend, the reader is referred to the web version of this article.)

calculation points in a material block. In our case, the distance between the calculation points across the thickness of the plate is 1.0E−06 m. The highest value of the distance between the calculation points in the plane of the plate is estimated at 1.2E−06 m. The horizon is assumed to be 3.0E-06 m (its maximum size being 3 × 1.2E−06 m), which is slightly lower than would result from the reasonable "soft" upper limit condition.

The calculations are done on a high-performance cluster under Linux. A production run requires about 3700 s employing 40 nodes with 24 cores each (Intel/Xeon). Larger values of the horizon would significantly increase the computation time. For example, increasing the horizon by two and three times would increase the computation time by 2.3 and 6.8 times. The following values were applied: h = 6.0E−06 m, time = 8.6E + 03 s; h = 12E−06 m, time = 2.5E + 04 s.

4. Numerical results

Two cases of plate material composition are considered. Case A is a plate material with a low content of Al_2O_3, and Case B is a plate material with a high content of Al_2O_3, Fig. 6(a) and (b), respectively. Damage progression in both cases is presented in Figs. 7 and 8. Damage progression results obtained with a high-velocity impact of 60 m/s for both cases of microstructure are compared qualitatively. The damage threshold is assumed to be 0.8. Points at which the damage threshold is exceeded are shown in Figs. 7 and 8. The color grey marks the Al_2O_3 phase, while the ZrO_2 phase is marked in blue. A comparison of the plate damage progression in Cases A and B demonstrates that the damage develops faster in the sample with a higher content of the ZrO_2 phase than of the Al_2O_3 phase.

A characteristic trend can be noted at the beginning of the impact process for both tested plates. An analysis of the data in Figs. 7(a, b) and 8(a, b) reveals that the damage is located along thin lines parallel to the striking edge of the plate. The most visible "bands" are located in the **X** region denoted by circles. However, this phenomenon can be observed along the entire edge. It can be explained by the appearance of short stress waves generated by the impact. The maximum values of the waves indicate a high damage factor of the material. As the process becomes more advanced, the thin lines

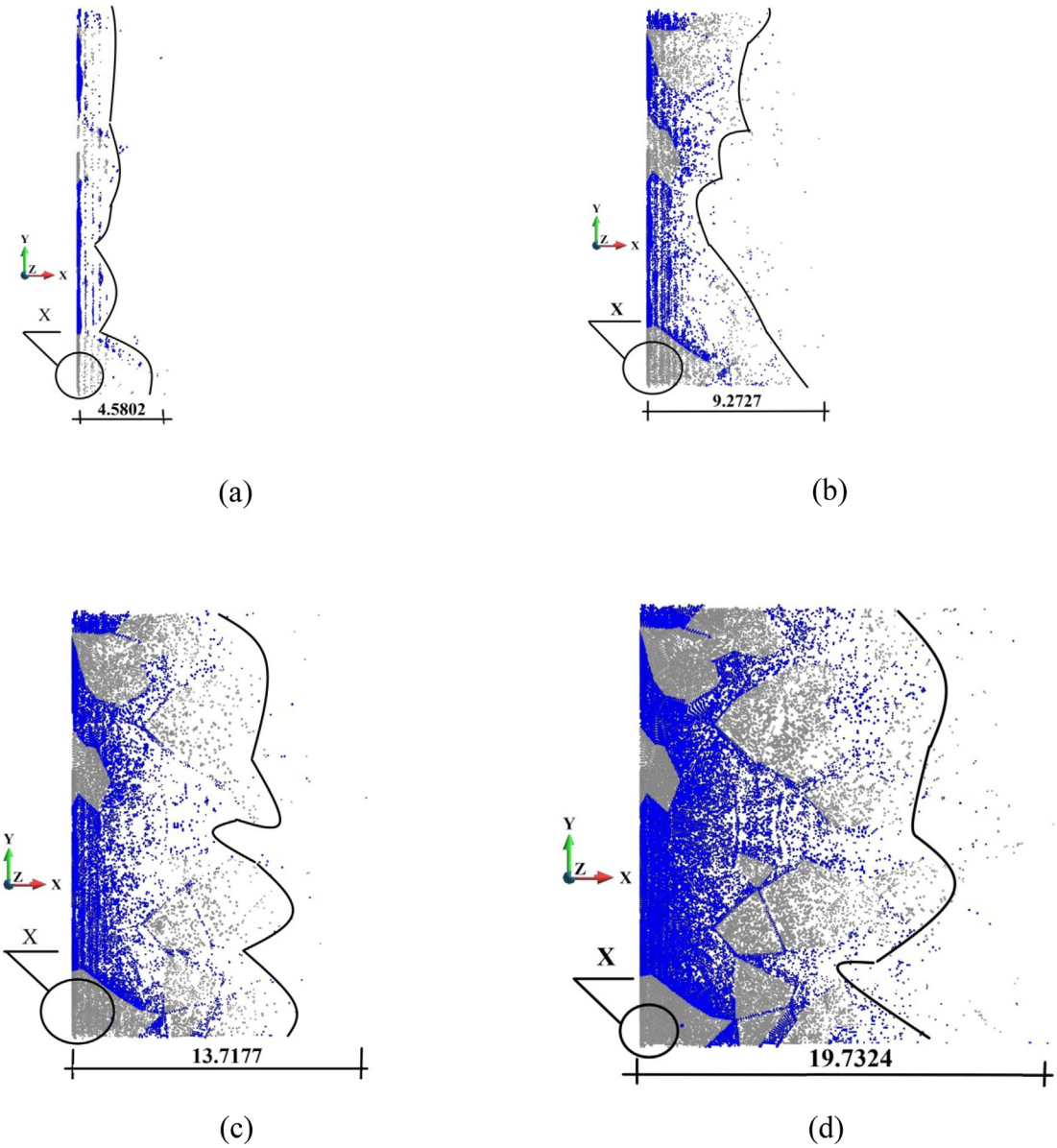

Fig. 7. Damage progression (dimension × 1.0E−5 m) versus time in Case A, for the impact velocity of 60 m/s: (a) 1.125E-08 s; (b) 2.375E−08 s; (c) 3.000E−07 s; (d) 4.000E−08 s.

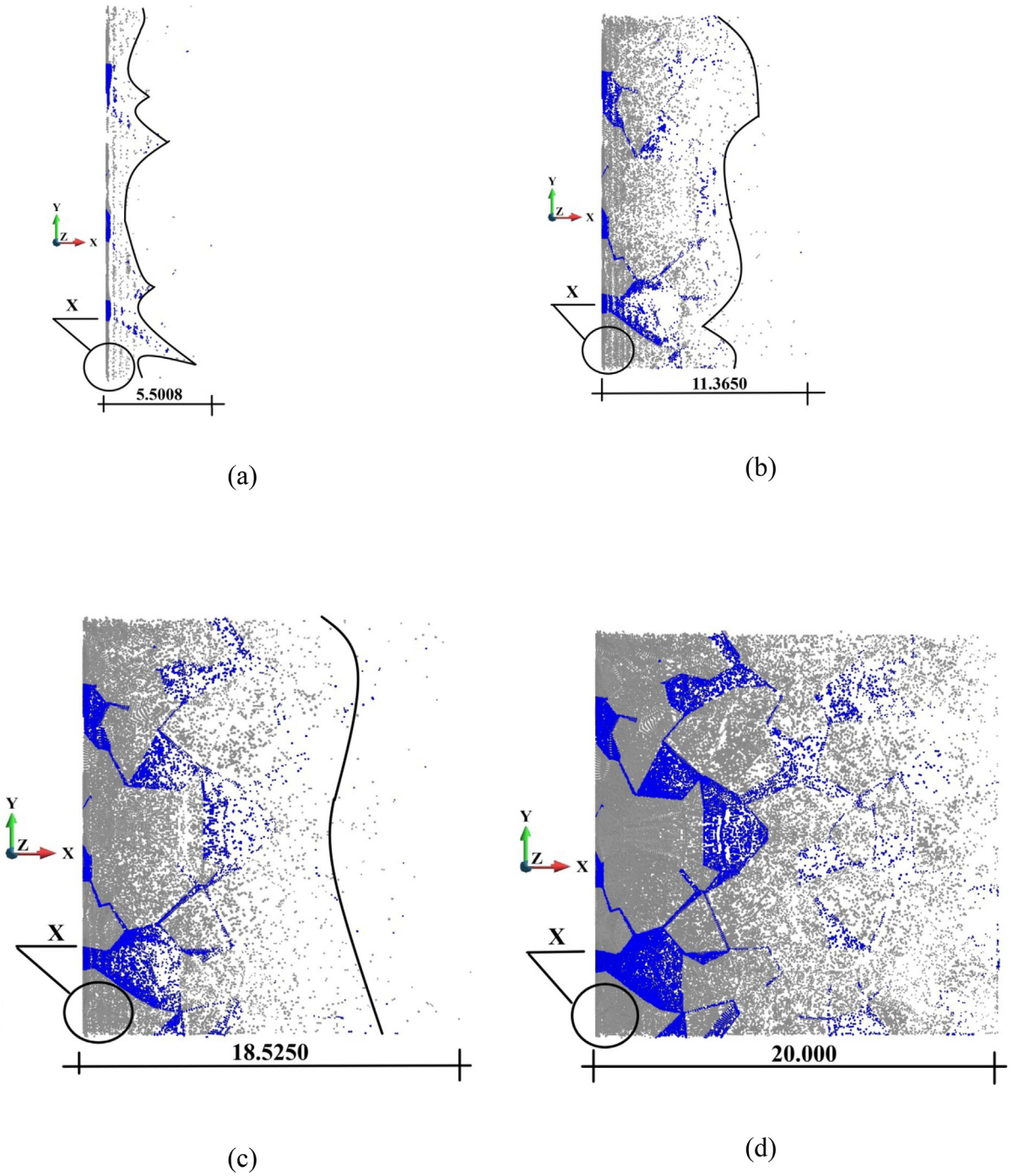

Fig. 8. Damage progression (dimension × 1.0E−5 m) versus time in Case B, for the impact velocity of 60 m/s: (a) 1.125E−08 s; (b) 2.375E−08 s; (c) 3.000E−07 s; (d) 4.000E−08 s.

marking damage disappear since the damage becomes massive, Fig. 7 (c, d) and 8 (c, d).

Further, it can be observed that as the damage progresses, the points where high values of the damage parameter are located become relatively sparse and precede the front face of massive damage. This trend can be observed in every image in Figs. 7 and 8. The damage progression is shown in Figs. 7 and 8 as the maximum distance of the damage from the striking damage than that in Case B. A comparison of the damage progression data in Figs. 7 and 8, considering the appropriate time instants, demonstrates that the damage ranges in Case A are 83.3%, 81.6%, 74.0% and 98.7% of those obtained in Case B.

Curves illustrating damage progression for the largest distance from the striking edge versus time for Cases A and B are plotted in Fig. 9. An analysis of the data in Fig. 9 reveals that in Case A the damage reaches the other edge of the plate only for the impact velocities of 40 m/s and 60 m/s. A different trend can be observed in Case B where the damage does not reach the other edge only when the impact velocity is 10 m/s. Moreover, the damage describing curves are steeper in Case B than in Case A, which means that the damage progresses faster in Case B. To verify the higher damage resistance of the microstructure in Case A, damage progression range plots are created for Cases A and B, taking into account the lowest and highest impact velocities, namely

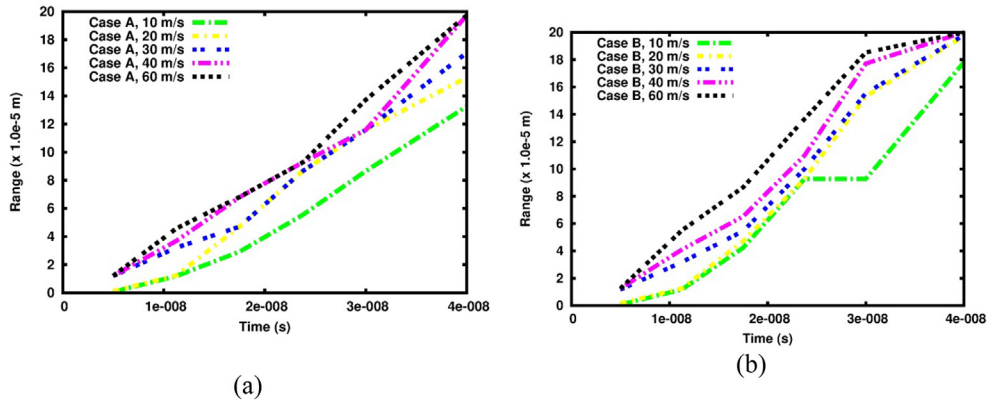

Fig. 9. Progression for the largest distance of the point d > 0.8 from the striking edge: (a) Case A; (b) Case B.

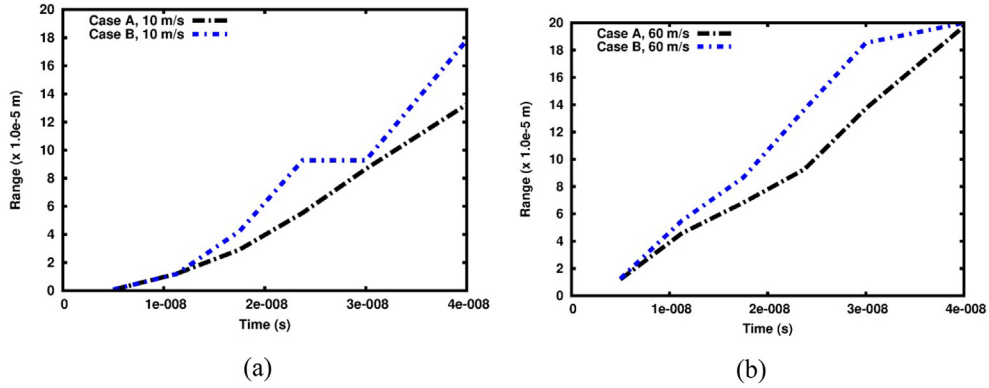

Fig. 10. Damage progression for the largest distance of the point d > 0.8 from the striking edge, for two impact velocities: (a) 10 m/s; (b) 60 m/s.

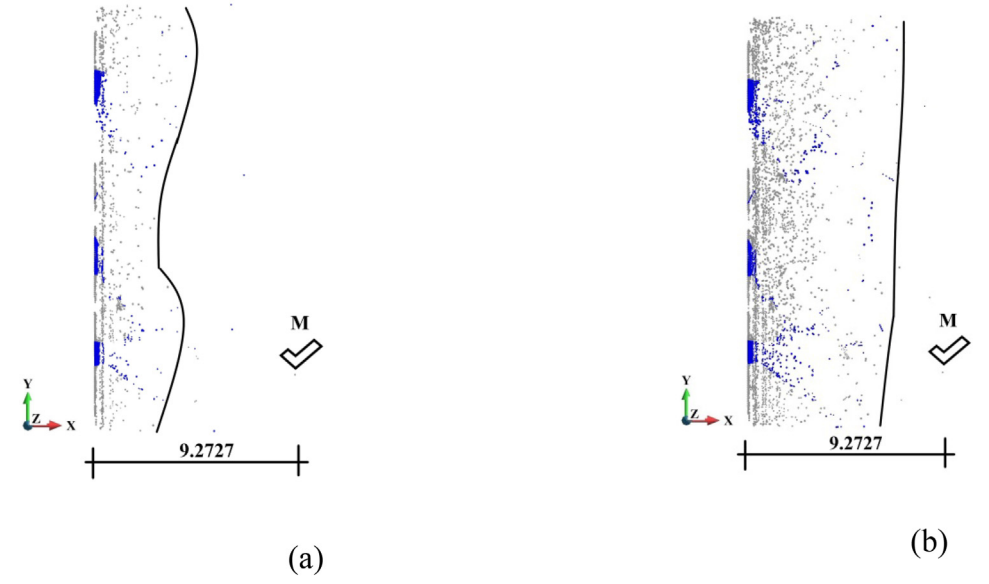

Fig. 11. Damage progression (dimension × 1.0E−5 m) for the largest distance of the point d > 0.8 from the striking edge, for the impact velocity of 10 m/s: (a) 2.375e−8s ; (b) 3.000e−8s.

10 m/s and 60 m/s, Fig. 10. It can be observed that the damage progresses faster in Case B than in Case A.

Let us now explain the phenomenon illustrated in Fig. 10(a), namely, the fact that at the time interval between 2.375E and 8s and 3.000E−8s, the damage range is the same. It appears that the damage range indicates the same point as that marked as Point M in Fig. 11. Point M is an early crack precursor. It occurs well before the front face of the damage developing during the afore-mentioned time interval.

It can be noted the damage is the highest in the mid-depth of the cross-section of the plate, Fig. 12. Damage evolution with time is evaluated at the points located at the middle of the plate's cross-section. Points A, B, C and D are indicated in Fig. 6. A comparison of the damage evolution at Points A, B, C and D for both analyzed cases, taking into account the moderate impact velocity of 30 m/s, is shown in Fig. 13. At each point, the damage occurs earlier in Case B than in Case A. At Points A, B, and D the damage is greater toward the end of the process in Case B than in Case A, while at Point C the damage values are similar for both microstructures under study. The comparison of the damage evolution curves confirms that the microstructure in Case B deteriorates faster than that in Case A.

A comparison of the damage evolution at all four considered points for both analyzed microstructures is presented in Figs. 14 and 15. It can be observed that the damage evolution curves at each point are qualitatively similar. The impact velocity has a minor effect on the time instant when the damage starts to grow. However, a significant difference between the obtained damage values can be observed toward the end of the process. The most considerable difference in damage can be observed at Point D for both analyzed microstructures.

Variations in the percentage of total damage with time obtained for the two analyzed polycrystalline microstructures are shown in Fig. 16. As previously, the dependences are shown for the impact velocity varying from 10 m/s up to 60 m/s. It can be observed that the damage growth is strongly nonlinear. The maximum total damage for Cases A and B is observed for the highest impact velocity of 60 m/s, and it amounts to 11.8% and 19.2%, respectively. However, an analysis of the relationship between the entire damage of the structure and the impact velocity at the observed time instants reveals that this relationship is practically linear, as shown in Fig. 17. The curves for Case B are steeper than those obtained for Case A. This means that the extent of microstructural damage in Case B is higher than in Case A.

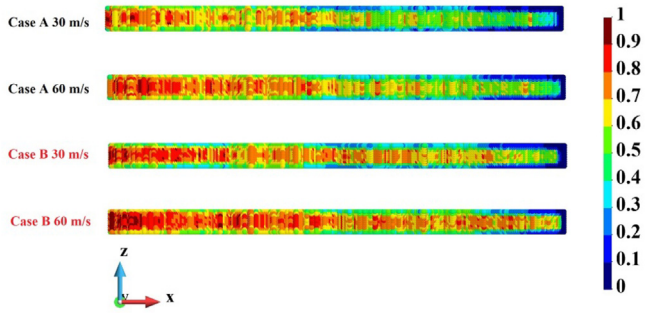

Fig. 12. Comparison of damage variable distributions in the mid-depth of the cross-section of the plate along the X-axis (at the midspan of the plate) for Case A and B.

5. Conclusions

Summing up the above considerations, it can be concluded that:

- Damage analysis of the impacting plates should be performed in three dimensions.
- The highest damage is concentrated close to the mid-depth of the cross-section, while the lowest is located close to the plate surface.
- The damage growth during impact, which is expressed as a percentage of the total damage of the plate, is strongly nonlinear.
- The damage occurs at an early stage of the process and is located sparsely, well before it becomes massive.
- In the tested impact velocity range, the traces of damage can be practically found over the entire plate irrespective of the impact velocity applied, which means that almost the entire plate is damaged to different extents.

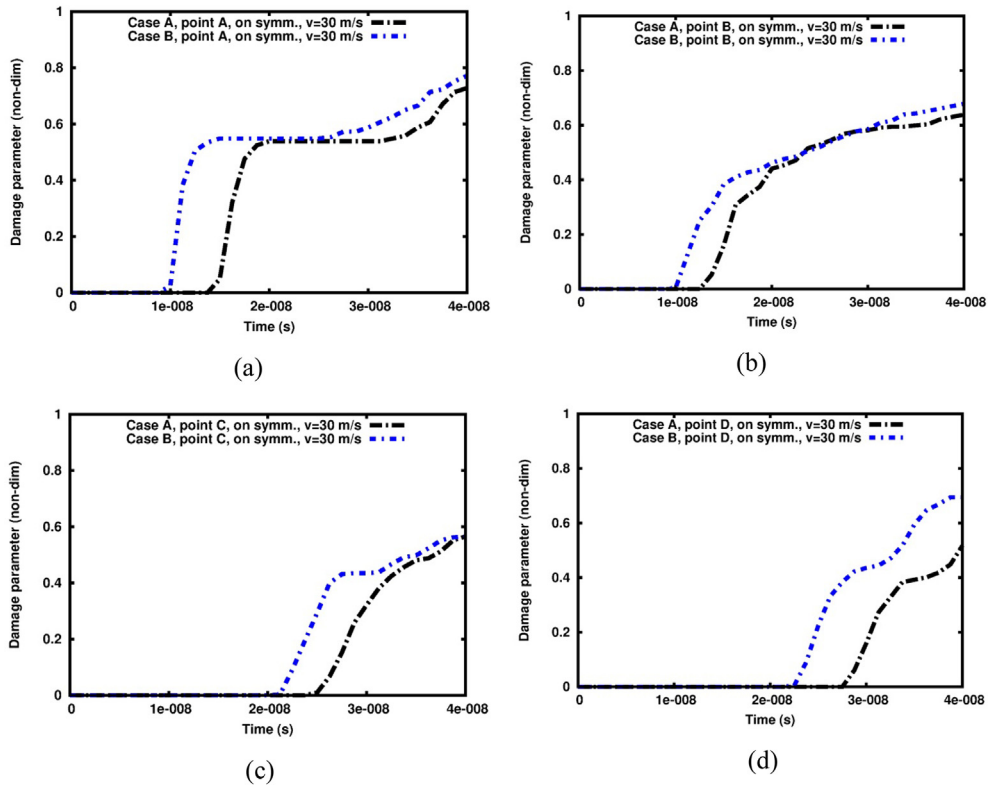

Fig. 13. Damage versus time in Cases A and B at points: (a) A; (b) B; (c) C; (d) D.

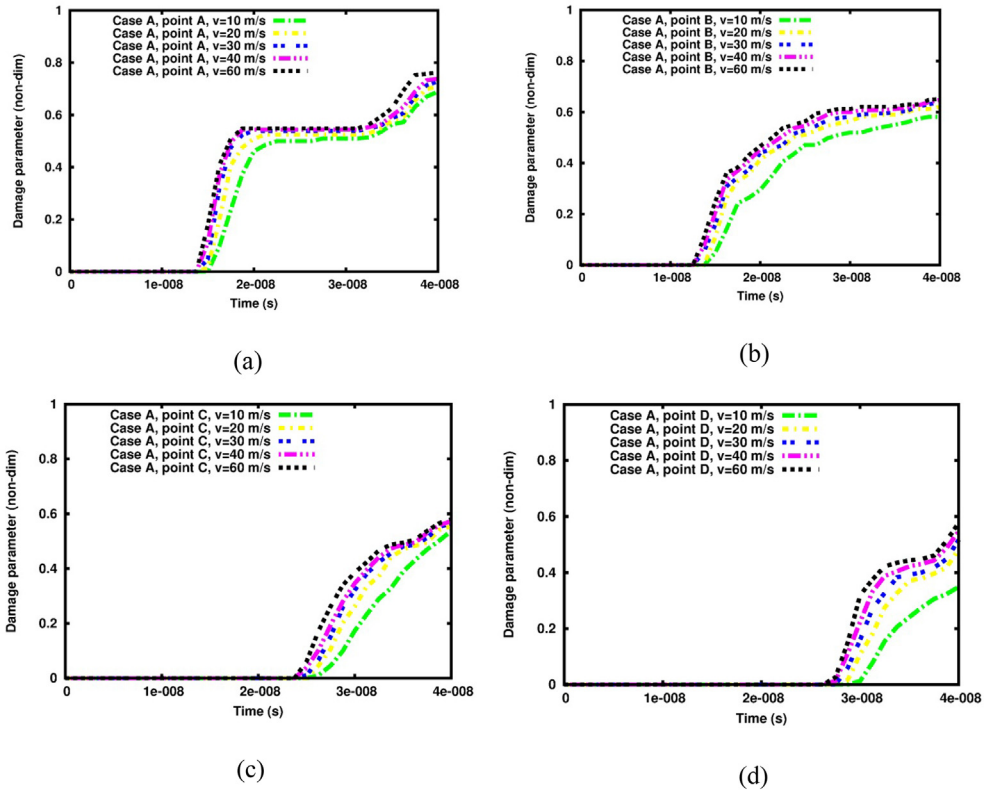

Fig. 14. Damage versus time for different impact velocities, Case A, points: (a) A; (b), B; (c) C; (d) D.

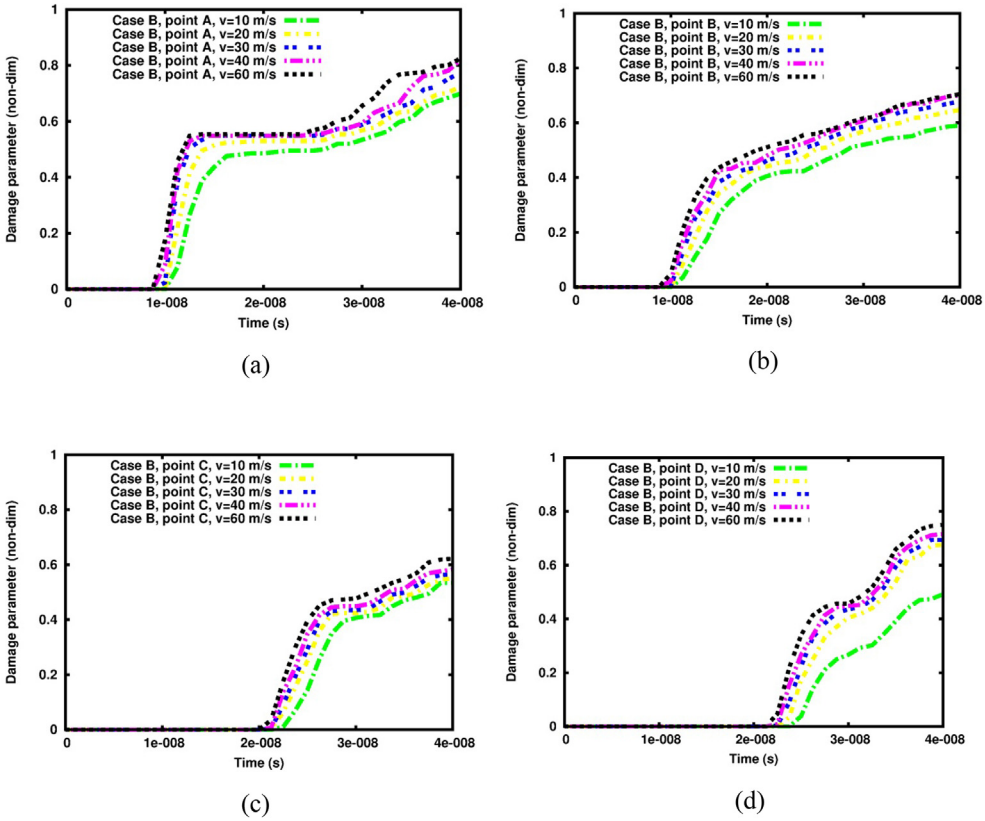

Fig. 15. Damage versus time for different impact velocities, Case B, points: (a) A; (b), B; (c) C; (d) D.

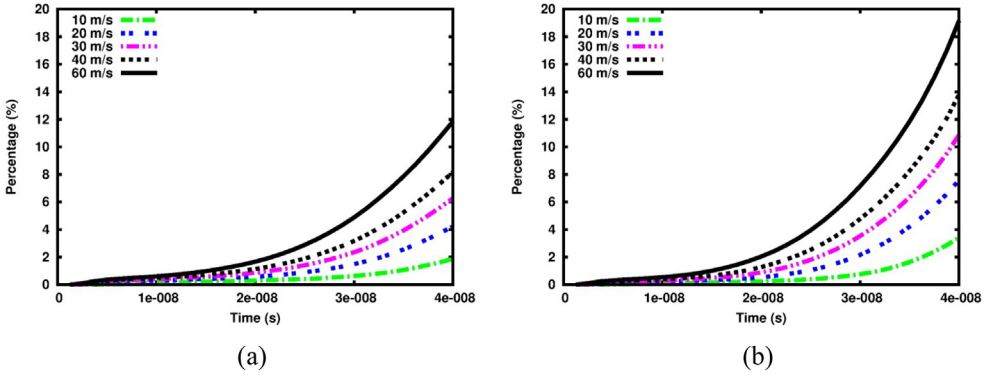

Fig. 16. Percentage of total damage versus time for different impact velocities, cases: (a) A; (b), B.

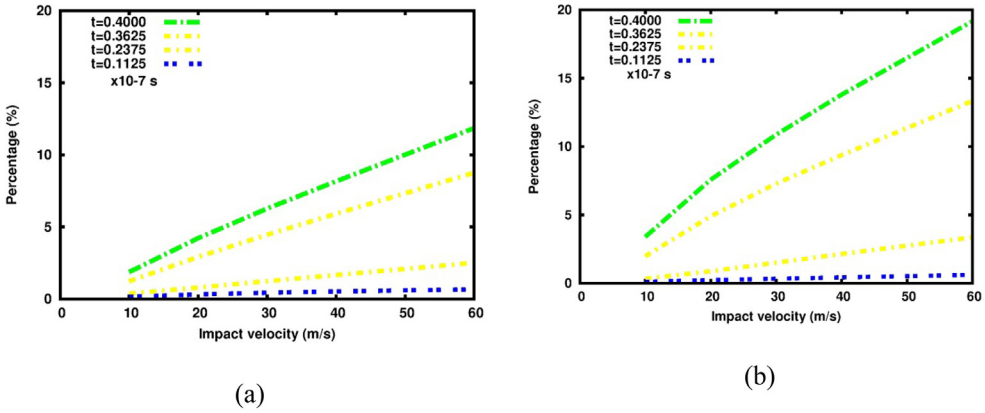

Fig. 17. Percentage of total damage at particular time instants versus impact velocity, cases: (a) A; (b), B.

- Regarding the dependence of total damage on impact velocity, it has been found that the damage variation is almost linear at particular time instants. This finding makes it possible to predict damage for different impact velocities using linear interpolation.
- At the beginning of the process, the damage forms lines that are parallel to the striking edge. We consider this phenomenon to be characteristic of the damage process for thin ceramic plates.
- The analysis confirms that Al_2O_3/ ZrO_2 composites with a high content of Al_2O_3 are less damage resistant than those with a high content of ZrO_2.

Moreover, the study has shown the presence of phenomena that are practically impossible to observe during experiments, for example, the concentration of damage in the form of strips parallel to the striking edge, occurring at the beginning of the process (time instant: 2.375E −08 s). Such observations broaden the knowledge about the material under study and inspire experimentalists to design new experiments.

The results of this study confirm the suitability of peridynamics for performance evaluation of ceramic composite components. However, it is necessary to use highly parallelized software and advanced computer clusters in order to obtain results within a reasonable time frame.

6. Data availability statement

Hereby the authors declare that: The raw/processed data required to reproduce these findings cannot be shared at this time due to legal or ethical reasons.

The raw/processed data required to reproduce these findings cannot be shared at this time due to technical or time limitations.

Declaration of Competing Interest

The authors declare that they have no known competing financial interests or personal relationships that could have appeared to influence the work reported in this paper.

Acknowledgements

This work was funded by the National Science Centre (Poland) under projects No 2016/21/B/ST8/01027 and No UMO-2019/33/B/ST8.

The calculations were done using PL-GRID national computational resources at the Academic Computer Centre Cyfronet in Krakow, Poland and the Interdisciplinary Centre for Mathematical and Computational Modeling, University of Warsaw, Poland. The license for the MSC Patran program was provided by the Academic Computer Centre in Gdańsk, Poland.

References

[1] Postek E, Sadowski T. Thermomechanical effects during impact testing WC/Co composite material. Compos Struct 2020;241:112054.
[2] Postek E, Sadowski T. Impact model of WC/Co composite. Compos Struct 2019;213:231–42.
[3] Postek E, Sadowski T. Temperature effects during impact testing of a two-phase metal-ceramic composite material. Materials 2019;12(10):1629. https://doi.org/10.3390/ma12101629.
[4] Sadowski T, Pankowski B. Numerical modelling of two-phase ceramic composite response under uniaxial loading. Compos Struct 2016;143:388–94.
[5] Fett T, Munz D. Mechanical Properties, Failure Behaviour, Materials Selection, Ceramics. 1st ed;. Heidelberg, New York: Springer: Berlin; 1999.
[6] Gömze LA, Gömze LN. Alumina-based hetero-modulus ceramic composites with extreme dynamic strength – phase transformation of Si_3N_4 during high speed

collision with metallic bodies *Építöanyag*. J Silicate Based Compos Mater 2009;61:38–42.
[7] Gömze LA, Gömze LN. Ceramic-based lightweight composites with extreme dynamic strength. IOP Conf. Ser.: Mater Sci Eng 2013;47:012033.
[8] Espinoza HD, Zavatteri PD. A grain level model for the study of failure initiation and evolution in polycrystalline brittle materials Part I: Theory and numerical implementation. Mech Mater 2003;35:333–64.
[9] Espinoza HD, Zavatteri PD. A grain level model for the study of failure initiation and evolution in polycrystalline brittle materials Part II: Numerical examples. Mech Mater 2003;35:365–94.
[10] Sadowski T, Golewski G. Effect of aggregate kind and graining on modelling of plain concrete under compression. Compos Mat Sci 2008;43(1):119–26.
[11] Ghosh D, Banda M, Akurati S, Kang H, Fakharizadeh VO. On the brittle fracture characteristics of lamella walls of ice-templated sintered alumina scaffolds and effects of platelets. Scripta Mater 2017;138:139–44.
[12] Sadowski T. Modelling of semi-brittle MgO ceramics behavior under compression. Mech Mater 1994;18:1–16.
[13] Sadowski T, Samborski S. Modelling of porous ceramics response to compressive loading. J Am Cer Soc 2003;86:2218–21.
[14] Rice RW. Porosity of ceramics. 1st ed. New York: Marcel Dekker Inc.; 1998.
[15] Sadowski T, Samborski S. Prediction of mechanical behaviour of porous ceramics using mesomechanical modelling. Comput Mat Sci 2003;29:512–7.
[16] Sadowski T, Samborski S. Development of damage state in porous ceramics under compression. Comput Mater Sci 2008;43(1):75–81.
[17] Boniecki M, Sadowski T, Gołebiewski P, Węglarz H, Piątkowska A, Romaniec M, et al. Mechanical properties of alumina/zirconia composites. Cer. Int. 2020;46:1033–9.
[18] Sadowski T, Marsavina L. Multiscale modelling of two-phase Ceramic matrix Composites. Comput Mater Sci 2011;50(4):1336–46.
[19] Sadowski T. Gradual degradation in two-phase ceramic composites under compression. Comput Mat Sci 2012;64:209–11.
[20] Sadowski T, Marsavina L, Craciun M. Cracking of two-phase ceramics under uniaxial compression deformation. Eng Trans 2017;65:39–44.
[21] Winter M. Nanocrystalline ceramics, synthesis and structure, 1st ed.; Springer: Berlin, 2002.
[22] Koch CC, Ovid'ko IA, Seal S, Veprek S. Structural nanocrystalline materials: fundamentals and applications. Cambridge Univ. Press: Cambridge, 2007.
[23] Suresh S. Mortensen, A. Fundamentals of functionally graded materials, 1st ed.; The University Press: Cambridge, 1998.
[24] Saleh B, Jiang J, Fathi R, Al-hababi T, Xu Q, Wang L, et al. 30 Years of functionally graded materials: An overview of manufacturing methods, applications and future challenges. Compos Part B 2020;201:108376. https://doi.org/10.1016/j.compositesb.2020.108376.
[25] Sadowski T, Boniecki M, Librant Z, Nakonieczny K. Theoretical prediction and experimental verification of temperature distribution in FGM cylindrical plates subjected to thermal shock. Int J Heat Mass Trans 2007;50(21-22):4461–7.
[26] Sadowski T, Nakonieczny K. Thermal shock response of FGM cylindrical plates with various grading patterns. Comput Mater Sci 2008;43(1):171–8.
[27] Clayton JD, Knap J. Geometric micromechanical modelling of structure changes, fracture and grain boundary layers in polycrystals. J Micromech Molecular Phys 2018;3:1840001.
[28] Bîrsan M, Sadowski T, Marsavina L, Linul E, Pietras D. Mechanical behavior of sandwich composite beams made of foams and functionally graded materials. Int J Solids Struct 2013;50(3-4):519–30.
[29] Sadowski T, Golewski P. The influence of quantity and distribution of cooling channels of turbine elements on level of stresses in the protective layer TBC and the efficiency of cooling. Comput Mater Sci 2012;52(1):293–7.
[30] Sadowski T, Golewski P. Detection and numerical analysis of the most efforted places in turbine blades under real working conditions. Comput Mater Sci 2012;64:285–8.
[31] Nakonieczny K, Sadowski T. Modelling of 'thermal shocks' in composite materials using a meshfree FEM. Comput Mater Sci 2009;44(4):1307–11.
[32] Sadowski T, Ataya S, Nakonieczny K. Thermal analysis of layered FGM cylindrical plates subjected to sudden cooling process at one side – comparison of two applied methods for problem solution. Comput Mater Sci 2009;45(3):624–32.
[33] Sadowski T, Birsan M, Pietras D. Numerical analysis of multilayered and FGM structural elements under mechanical and thermal loads. Comparison of the finite elements and analytical models. Arch Civ Mech Eng 2015;15:1180–92.
[34] Sadowski T, Neubrand A. Estimation of the crack length after thermal shock in FGM strip. Int J Fract 2004;127(2):L135–40.
[35] Ivanov IV, Sadowski T, Pietras D. Crack propagation in functionally graded strip under thermal shock. Europ Phys J Spec Top 2013;222(7):1587–95.
[36] Burlayenko VN, Altenbach H, Sadowski T, Dimitrova SD, Bhaskar A. Modelling functionally graded materials in heat transfer and thermal stress analysis by means of graded finite elements. Appl Math Model 2017;45:422–38.
[37] Sigl LS, Fischmeister HF. On the fracture toughness of cemented carbides. Acta Metall 1988;36(4):887–97.
[38] Ravichandran KS. Fracture toughness of two phase WC-Co cermets. Acta Metal Mater 1994;42(1):143–50.
[39] Hönle S, Schmauder S. Micromechanical simulation of crack growth in WC/Co using embedded unit cells. Comput Mater Sci 1998;13(1-3):56–60.
[40] Sadowski T, Nowicki T. Numerical investigation of local mechanical properties of WC/Co composite. Comput Mater Sci 2008;43(1):235–41.
[41] Felten F, Schneider GA, Sadowski T. Estimation of R-curve in WC/Co cermet by CT test. Int J Ref Mat Hard Mat 2008;26(1):55–60.
[42] Liu X, Wang H, Wang L, Hou C, Song X, Liu X, et al. *In situ* study of fracture behavior of ultrafine WC–Co cemented carbide. Mat Res Letters 2017;5(1):55–60.
[43] Sadowski T, Hardy SJ, Postek EW. Prediction of the mechanical response of polycrystalline ceramics containing metallic intergranular layers under uniaxial tension. Comput Mater Sci 2005;34(1):46–63.
[44] Sadowski T, Hardy S, Postek E. A new model for the time-dependent behaviour of polycrystalline ceramic materials with metallic inter-granular layers under tension. Mater Sci Eng A 2006;424(1-2):230–8.
[45] Sadowski T, Postek E, Denis Ch. Stress distribution due to discontinuities in polycrystalline ceramics containing metallic inter-granular layers. Comput Mater Sci 2007;39(1):230–6.
[46] Postek E, Sadowski T. Assessing the influence of porosity in the deformation of metal-ceramic composites. Compos Interf 2011;18(1):57–76.
[47] Marsavina L, Sadowski T. Stress Intensity Factors for an interface kinked crack in a bi-material plate loaded normal to the interface. Int J Frac 2007;145(3):237–43.
[48] Nemat-Nasser S, Horii M. Micromechanics: overall properties of the heterogeneous materials. 1st ed.;. Amsterdam – New York – Oxford – Tokyo: Elsevier:; 1999.
[49] Gross D, Seelig T. Fracture mechanics with an introduction to micromechanics. 1st ed. Berlin- Heidelberg: Springer; 2006.
[50] Kassner ME, Nemat-Nasser S, Suo Z, Bao G, Barbour JC, Brinson LC, et al. New directions in mechanics. Mech Mat 2005;37(2-3):231–59.
[51] Kachanov M, Sevostianov I. Micromechanics of materials, with Applications. 1st ed. Heidelberg, New York, London: Springer; 2018.
[52] Kachanov M, Sevostianov I. Effective Properties of Heterogeneous materials. 1st ed. Dordrecht, Heidelberg, New York, London: Springer; 2013.
[53] de Borst R, Sadowski T, editors. Lecture notes on composite materials. Wien-New York: Springer-Verlag; 2008.
[54] de Borst R. Challenges in computational materials science, multiple scales, multi-physics and evolving discontinuities. Comput Mater Sci 2008;43(1):1–15.
[55] Favata A, Trovalusci P, Masiani R. A multiphysics and multiscale approach for modeling microcracked thermo-elastic materials. Comput Mater Sci 2016;116:22–31.
[56] Tkalich D, Cailletaud G, Yastrebov VA, Kane A. A micromechanical constitutive modeling of WC hardmetals using finite-element and uniform field models. Mech Mater 2017;105:166–87.
[57] Marsavina L, Sadowski T. Fracture parameters at bi-material ceramic interfaces under bi-axial state of stress. Comput Mater Sci 2009;45(3):693–7.
[58] Marsavina L, Sadowski T. Kinked crack at a bi-material ceramic interface – Numerical determination of fracture parameters. Comput Mater Sci 2009;44(3):941–50.
[59] Okada A. Ceramic technologies for automotive industry: Current status and perspectives. Mater Sci Eng B 2009;161:182–7.
[60] Pittari J, Subhash G, Zheng J, Halls V, Jannotti P. The rate-dependent fracture toughness of silicon carbide- and boron carbide-based ceramics. Eur Ceram Soc 2015;35(16):4411–22.
[61] Ohji T, Singh M. Engineered Ceramics: Current Status and Future Prospects. 1st ed. New York: Wiley; 2015.
[62] Rogula D. Nonlocal theory of material media. 1st ed. Wien, New-York: Springer; 1982.
[63] Kunin A. Elastic media with microstructure, one dimensional models. 1st ed. Berlin, Heidelberg, New-York: Springer; 1982.
[64] Eringen AC. Nonlocal continuum field theories. 1st ed. New-York, Berlin, Heidelberg: Springer; 2001.
[65] Silling SA. Reformulation of elasticity theory for discontinuities and long-range forces. J Mech Phys Solids 2000;48(1):175–209.
[66] Silling SA, Askari E. A meshfree method based on the peridynamic model of solid mechanics. Comput Struct 2005;83(17-18):1526–35.
[67] Postek E, Pęcherski R, Nowak Z. Peridynamic simulation of crushing processes in copper open-cell foam. Arch Metall Mater 2019;64:1603–10.
[68] Silling SA, Epton M, Weckner O, Xu J, Askari E. Peridynamic states and constitutive modeling. J Elasticity 2007;88(2):151–84.
[69] https://www.azom.com/properties.aspx?ArticleID = 52 (access 12th Jan. 2021)
[70] https://www.azom.com/properties.aspx?ArticleID = 133 (access 12th Jan. 2021)
[71] Parks ML, Littlewood DJ, Mitchell JA, Silling SA. Peridigm users'guide. Sandia National Laboratories: Sandia report; 2012.
[72] Liu M, Wang Q, Lu W. Peridynamic simulation of brittle-ice crushed by a vertical structure. Int J Nav/ Arch Ocean 2017;9(2):209–18.
[73] Ha YD, Bobaru F. Studies of dynamic crack propagation and crack branching with peridynamics. Int J Fract 2010;162(1-2):229–44.
[74] Madenci E, Oterkus E. Peridynamic Theory and Its Applications. 1st ed. New York: Springer; 2014.
[75] Open Source Peridigm program repository https://github.com/peridigm/peridigm (access 12th Jan. 2021)
[76] Huang C-Y, Chen Y-L. Design and impact resistant analysis of functionally graded Al_2O_3-ZrO_2 ceramic composite. Mater Des 2016;91:294–305.
[77] Postek E, Sadowski T, Boniecki M. Impact of brittle composites: Peridynamics modelling. Mater Today-Proc 2021. In press, available online 8th Feb 2021.
[78] Littlewood DJ. Simulation of dynamic fracture using peridynamics, finite element modeling, and contact, Proceedings of the ASME 2010 International Mechanical Engineering Congress & Exposition, Vancouver, Canada, Nov. 12-18, 2010, IMECE2010-40621, 9 pages.
[79] Silling SA, Lehoucq RB. Convergence of peridynamics to classical elasticity theory. J Elast 2008;93(1):13–37.
[80] Silling SA, Lehoucq RB. Peridynamics theory of solid mechanics. Adv Appl Mech 2010;44:73–168.

[81] Littlewood DJ. Introduction to peridynamic modeling and applications.
[82] https://www.osti.gov/servlets/purl/1511976 (accessed on 12th January 2021).
[83] Macek WM, Silling SA. Peridynamics via finite element analysis. Finite Elem Anal Des 2007;43:1168–78.
[84] SIERRA Solid Mechanics Team. Sierra/SolidMechanics 4.36 user's guide. SAND 2015-2199, Sandia National Laboratories, Albuquerque, NM and Livermore, CA.
[85] LS Dyna, https://www.ansys.com/products/structures/ansys-ls-dyna (accessed on 12th January 2021).
[86] Abaqus 6.13, https://www.3ds.com/products-services/simulia/ (accessed on 12th January 2021).
[87] Isiet M, Mišković I, Mišković S. Reformulation Review of peridynamic modelling of material failure and damage due to impact. Int J Impact Eng 2021;147:103740. https://doi.org/10.1016/j.ijimpeng.2020.103740.
[88] Ye LY, Wang C, Chang X, Zhang HY. Propeller-ice contact modeling with peridynamics. Ocean Eng 2017;139:54–64.
[89] Freimanis A, Kaewunruen S. Peridynamic analysis of rail squats. Appl Sci 2018;8 (11):2299. https://doi.org/10.3390/app8112299.
[90] Littlewood DJ, Volgler T. Modeling dynamic fracture with peridynamics, Finite Element Modeling and Contact, 11th US National Congress on Computational Mechanics, July 25-28, 2011, https://www.osti.gov/servlets/purl/1106568 (accessed on 12th January 2021).
[91] Belinha J, Araujo AL, Ferreira AJM, Dinis LMJS, Natal Jorge RM. The analysis of laminated plates using disti advanced discretization meshless techniques. Compos Struct 2016;143:165–79.
[92] Caliri MF, Ferreira AJM, Tita V. A review on plate and shell theories for laminated and sandwich structures highlighting the Finite Element Method. Compos Struct 2016;156:63–77.
[93] Sing A, Das S, Altenbach H, Craciun EM. Semi-infinite moving crack in an orthotropic strip sandwiched between two identical half planes. ZAMM 2020;100:1–13.
[94] Singh A, Das S, Craciun E-M. Effect of thermomechanical loading on an edge crack of finite length in an infinite orthotropic strip. Mech Comp Mat 2019;55 (3):285–96.
[95] Golewski P, Sadowski T. Description of thermal protection against heat transfer of carbon fiber reinforced plastics (CFRP) coated by stiffened ceramic mat (TBC). Compos Struct 2019;229:111489. https://doi.org/10.1016/j.compstruct.2019.111489.
[96] Sadowski T, Golewski P, Craciun E. Internal structure influence on the impact strength and dynamic fracture toughness of hybrid polymer matrix composites with integrated elastomer interlayers. Compos Struct 2021;258:113375. https://doi.org/10.1016/j.compstruct.2020.113375.
[97] Pietras D, Linul E, Sadowski T, Rusinek A. Out-of-plane crushing response of aluminum honeycombs in-situ filled with graphene-reinforced polyurethane foam. Compos Struct 2020;249:112548. https://doi.org/10.1016/j.compstruct.2020.112548.
[98] Bîrsan M, Pietras D, Sadowski T. Determination of effective stiffness properties of multilayered composite beams. Continuum Mech Thermodyn 2021 (on-line) https://doi.org/10.1007/s00161-021-01006-2
[99] Burlayenko VN, Sadowski T, Altenbach H. Efficient free vibration analysis of FGM sandwich flat panels with conventional shell elements. Mechanics of Advanced Materials and Structures, 2021 (on-line) https://doi.org/10.1080/15376494.2021.1909191
[100] Sadowski T, Bec J. Effective properties for sandwich plates with aluminium foil honeycomb core and polymer foam filling - Static and dynamic response. Comput. Mater. Sci. 2011;50:1269–75.
[101] Golewski G, Sadowski T. The fracture toughness KIIIc of concretes with F fly ash during tprsional loading. Constr. Build. Mater. 2017;143:444–54.
[102] Sadowski T, Golewski G. A failure analysis of concrete composites incorporating fly ash during torsional loading. Compos. Struct. 2018;183:527–35.
[103] Linul E, Marsavina L, Voiconi T, Sadowski T. Study of factors influencing the mechanical properties of polyurethane foams under dynamic compression. Journal of Physics: Conference Series 2013;451:012002.
[104] Burlayenko V, Sadowski T. A numerical study of the dynamic response of sandwich plates initially damaged by low-velocity impact. Comput. Mater. Sci. 2012;52:212–6.